Geophysical Research Letters

Supporting information for

A new record of Atlantic sea surface salinity from 1896 to 2013 reveals the signatures of climate variability and long-term trends

Andrew R. Friedman[1], Gilles Reverdin[1], Myriam Khodri[1], and Guillaume Gastineau[1]

[1]Sorbonne-Universités, LOCEAN, CNRS/IRD/UPMC/MNHN, Paris, France

Corresponding authors: Gilles Reverdin (gilles.reverdin@locean-ipsl.upmc.fr), and Andrew R. Friedman (andrew.friedman@locean-ipsl.upmc.fr)

Updated 24 March 2017

Contents

Text S1: SSS uncertainties and errors

S1.1 Collection and measurement uncertainties

The uncertainty of SSS data is influenced by the collection method and by how SSS is estimated. The issue of the collection method is related to potential inhomogeneities due to stratification: changes in the depth of water sampling could induce average changes in SSS in net evaporative regions *[Asher et al., 2014; Yu, 2010]* or in net precipitative regions *[Anderson & Riser, 2014; Boutin et al., 2014]*. Upper estimates of these averaged effects are 0.02 PSS-78 between 5m and a few cm depth *[Boutin et al., 2014]*. How samples were collected and how they were stored before being measured is also very important *[Reverdin et al., 1994]*, as well as how thermosalinograph records were calibrated/corrected. There is also the uncertainty resulting from the evolution since the late 19th century in the standards against which the measurements are calibrated or in the method used to provide an estimate of salinity (from chlorinity titration to conductivity measurements). For the Atlantic sector surface waters that we consider, these instrumental sources of error are expected to be less than 0.02 PSS-78 *[Fofonoff, 1985]*. We do not find evidence of jumps with the major instrumental or measurement changes which would happen for example in 1977, in the mid 1990s, or in the early 2000s.

Some of the datasets have been adjusted based on intercomparisons in the northeast Atlantic and North Sea, as described in *Reverdin et al.* [*1994*]. These corrections are large for

some sets until the 1960s, and there could be remaining biases. For example, we have less confidence in some of the early data collected from ships of opportunity in the tropics. We eliminated the most flawed data, and then corrected the surface samples based on comparison with Nansen cast data mostly near Europe. However, this could potentially leave remaining errors in the warmer tropics, particularly for 1910–1914, with the exception of higher-quality cruise data from 1911 described in *Reverdin* [*1996*].

S1.2 Gridbox uncertainties

Within each box, error terms for each season are estimated similarly to the standard error of the mean, but using squared deviations from the median (we did not find large differences between the two estimates, but the median estimates were a little less noisy). We also remove large seasonal outliers with a threshold of 0.6 PSS-78, larger in regions of fronts or high variability (based to be at least 2 standard deviations). The seasonal error terms are 1-2-1 root-mean-square (RMS) averaged in time, and the yearly error term is estimated as the weighted RMS average of the seasonal errors. We find that the different seasonal time series are generally well-correlated, as was earlier found in the northeastern subpolar gyre *[Reverdin, 2010]*.

The total number of boxes with data for each season per year is shown in **Fig. S6a**, out of a maximum of 128 (32 boxes × 4 seasons). Note that this coverage is computed after the 1-2-1 filter is applied. Coverage is below 32 seasonal boxes per year from 1917–1919 and 1941–46. 1943 has zero coverage, and 1944 has only four seasonal boxes. The corresponding spatial totals are shown in **Fig. S6c**, out of a maximum of 472 (118 years × 4 seasons). For boxes north of 5°N, the time series have data for most years, except for some of the WWI and WWII years, which we interpolate linearly. The time series south of 5°N have much longer data gaps as well as periods with insufficient accuracy, in particular before 1899, 1916–1921, and 1941–1955. For these 6 southernmost boxes, we fill short gaps (5 years or less) by linear interpolation, and fill longer gaps by regressing anomalies from the one or two highest-correlated nearby boxes (depending on the nearby data availability and correlation strength). The error term during the interpolated periods is estimated as the standard deviation of the long-term yearly time series (which is probably an overestimate). The error terms of the regional time series (TATL, NATL, and NTROP) are constructed by RMS averaging the error terms of their constituent individual boxes.

Fig. S6b presents an estimate of the average annual (1-2-1 filtered) gridbox uncertainty. For each gridbox, a fractional error time series is calculated as the annual error term divided by the error term during 1943, when there was no coverage and the error is maximum. The individual fractional box error terms are then area-averaged. This fractional error is strongly negatively correlated with the seasonal coverage index in **Fig. S6a** ($r = -0.95$), but it also depends on the uncertainties in the individual measurements. The gridbox temporal averages of these fractional errors are shown in **Fig. S6d**.

In some boxes, some seasons are excluded where they present much higher error estimates or lower correlations with other seasons (generally $r<0.6$). For example, the late rainy season September–November was excluded from the two boxes from 5°–15°N/ 25°–50°W and 15º–20ºN/ 55º–75ºW, due to large gaps and uncorrelated signals with the other seasons. Near the equator in the west in two boxes (5ºS–4ºN/ 20º–35ºW and 10ºS–5ºS/ 20º–35ºW), the rainy season March–May was excluded. The winter season December–February was excluded from the Labrador Sea, since it has less than half of the time with winter sampling, in particular none before 1940. Examples from three different regions are shown in **Fig. S7**: the Labrador Sea (45°–48/56°W, 50°–59°N; **Fig. S7b**), the western subtropical gyre

(55°–75°W, 20°–27°N; **Fig. S7c**), and the ITCZ (25–50°W, 5–15°N; **Fig. S7d**). December–February is not included in the annual time series in **Fig. S7b,** and September–November is not included in the annual average time series in **Fig. S7d.**

Additionally, we note that three pairs of boxes were calculated with small regions of overlap (< 10% box area): (30°–47°W, 20°–30°N)/(20°–35°W, 25°–35°N); (35°–55°W, 30°–38°N)/(20°–40°W, 35°–40°N); and (20°–35°W, 5°S–4°N)/(34°–45°W, 3°S–5°N). In these cases, the shared area is divided equally between the overlapping boxes in subsequent calculations, and the box boundaries are represented as diagonal lines.

S1.3 Atlantic pattern amplification (PA) uncertainties

The Atlantic PA 95% confidence intervals (CIs) are calculated using the least squares regression standard errors of the Atlantic PA slope; note that this does not account for uncertainties in the zonal mean estimates. The 95% CIs of the temperature-scaled Atlantic PA coefficient are calculated using an error propagation approximation for ratios, by summing in quadrature the 95% CIs of the Atlantic PA coefficient and of the fractional GMST trend.

Supporting Figures

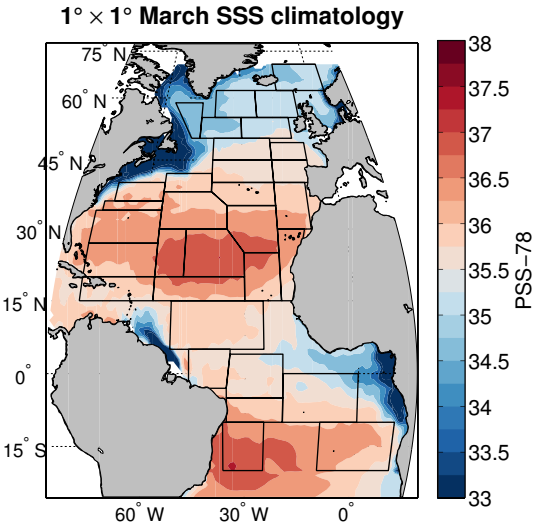

Figure S1. 1977–2013 objectively analyzed 1°×1° March SSS climatology, updated and extended to 70°N from *Reverdin et al. [2007],* in PSS-78. Earlier measurements were included north of 50°N, with no substantive differences at the 50°N boundary.

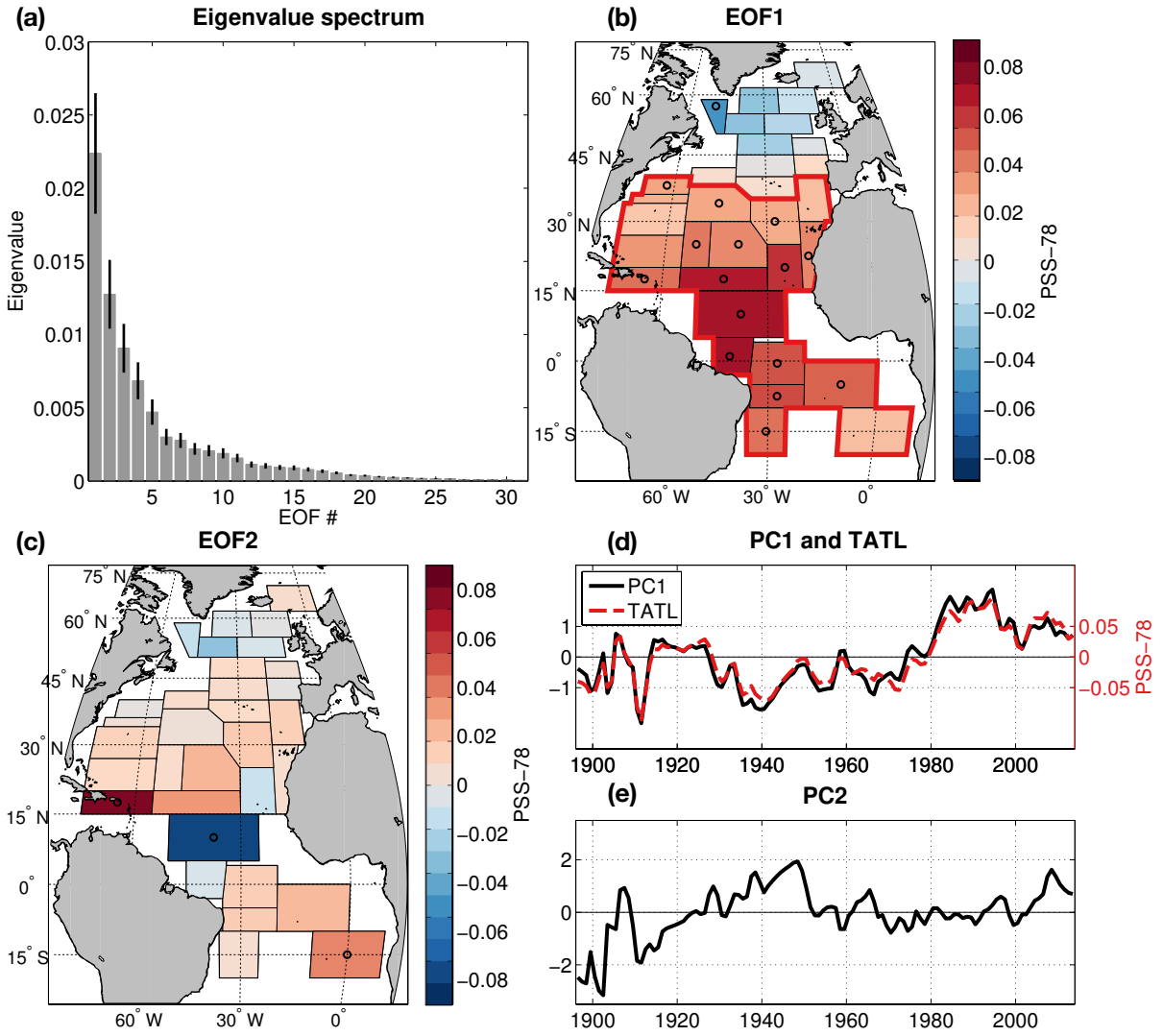

Figure S2: (a) SSS eigenvalue spectrum. The error bars indicate the 95% confidence error from *North et al. [1982]*. We assume 59 degrees of freedom (118 years / 2), to account for the autocorrelation induced by the 1-2-1 filter. (b) SSS EOF1, shown as the slope of SSS regressed onto normalized PC1 (to indicate typical amplitudes), in PSS-78. Circles indicate where the correlation with PC1 is significant at $p<0.05$. Red solid outline indicates the TATL region. (c) Same as (b), for EOF2. (d) PC1 (black solid, left axis) and TATL (red dashed, right axis) time series. (e) PC2 time series.

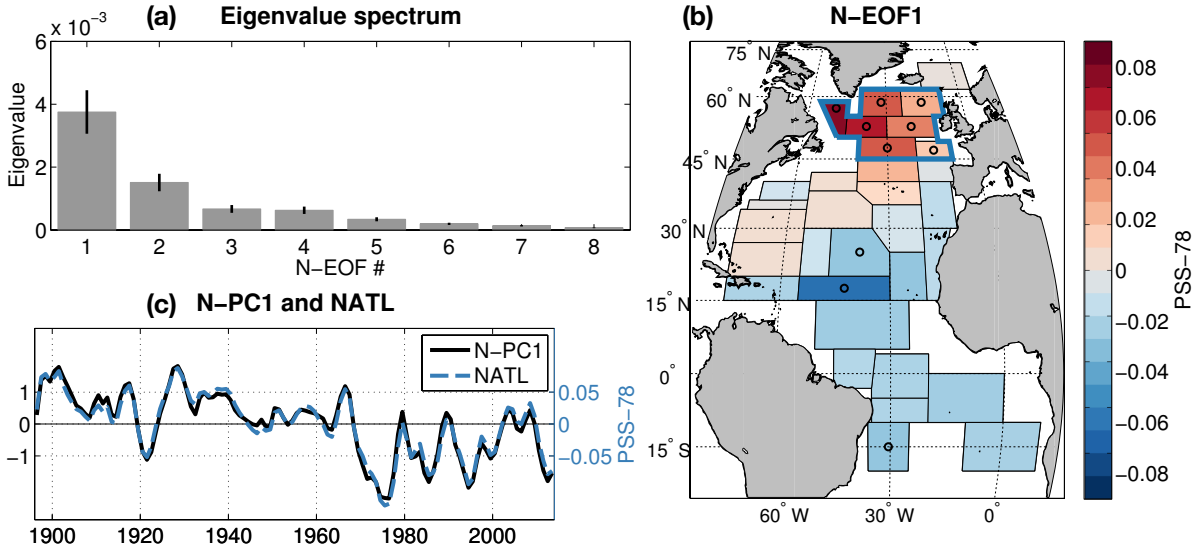

Figure S3: (a) Eigenvalue spectrum similar to **Fig. S2a**, but for SSS grid boxes north of 45ºN. (b) SSS N-EOF1 pattern, shown as the slope of SSS regressed onto normalized N-PC1, in PSS-78. Circles indicate where the correlation with N-PC1 is significant at $p<0.05$. Blue solid outline indicates NATL region. (c) N-PC1 (black solid, left axis) and NATL (blue dashed, right axis) time series.

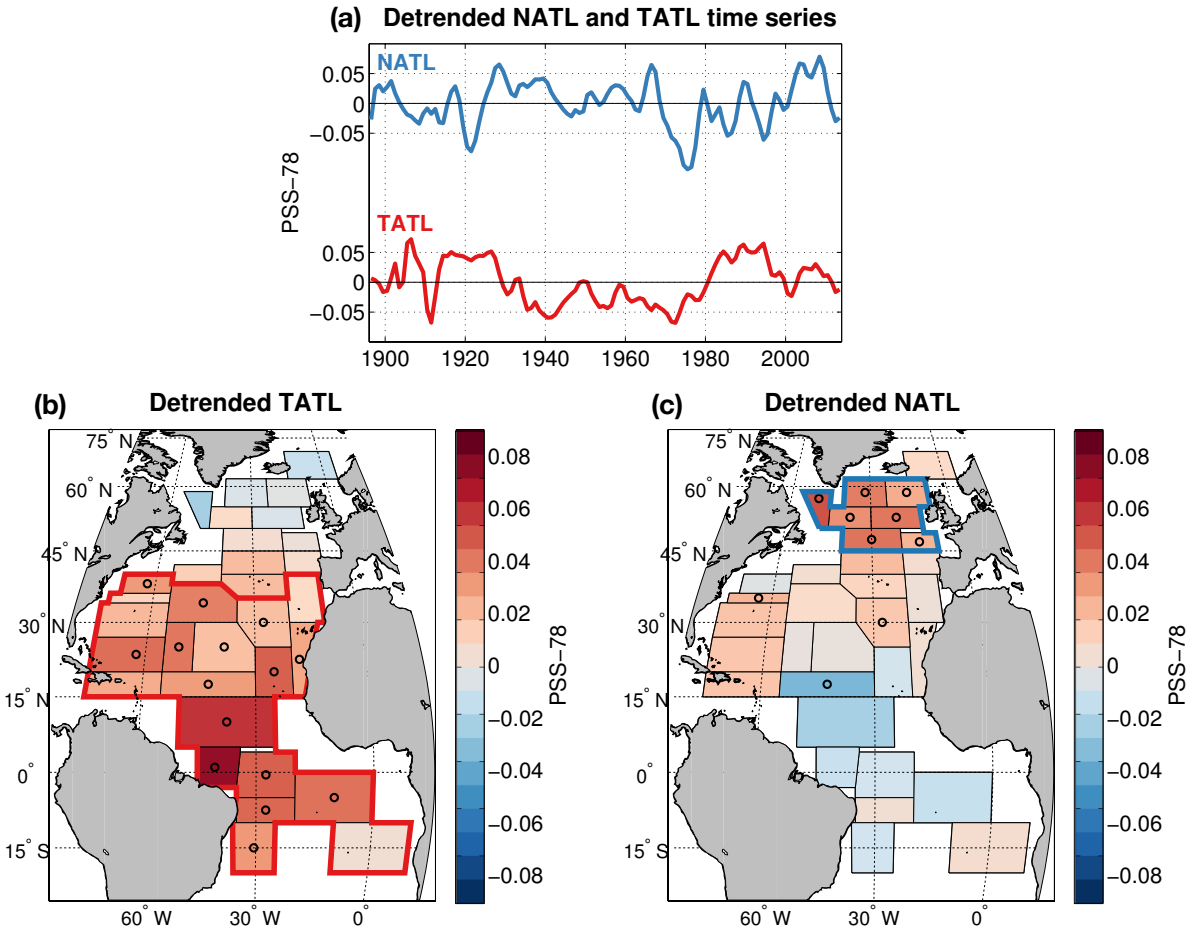

Figure S4. (a) Detrended NATL (top) and TATL (bottom) anomalies, in PSS-78. (b) Detrended TATL spatial pattern, shown as the slope of detrended SSS regressed onto the normalized detrended TATL time series, in PSS-78. Circles indicate where the correlation is significant at $p<0.05$. Red solid outline indicates the TATL region. (c) Same as (b), but for NATL.

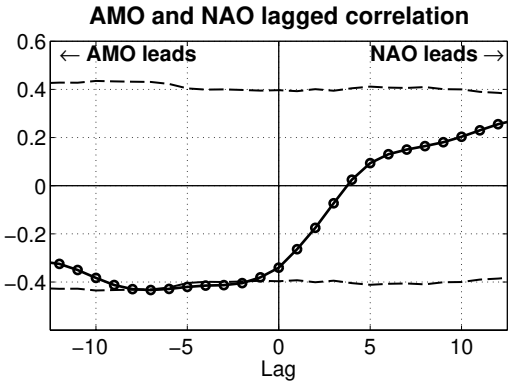

Figure S5. Lagged correlation of the AMO and NAO. The dashed lines show the 95% CIs.

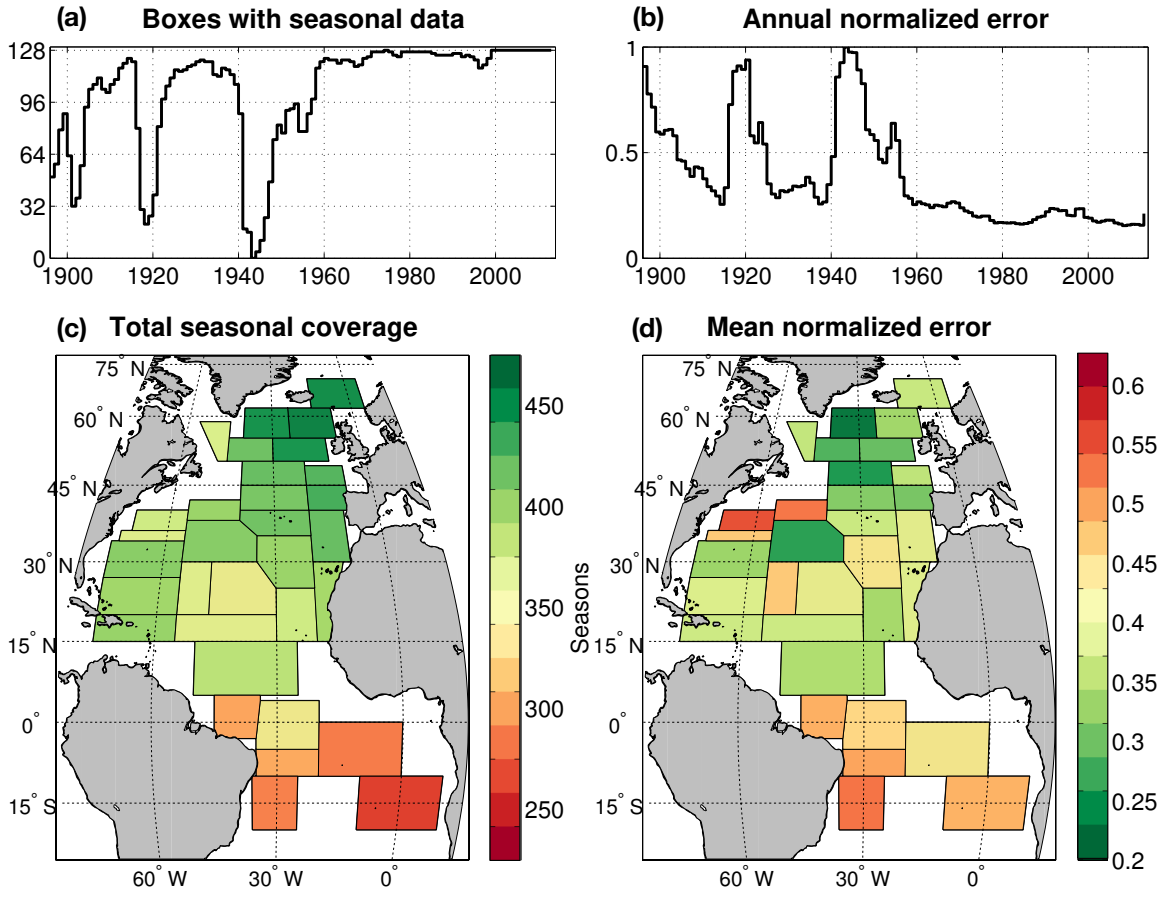

Figure S6. (a) Number of boxes with seasonal data per year, out of a maximum of 128. (b) Area-weighted normalized annual gridbox uncertainty, defined as the area-averaged gridbox error divided by the error in 1943. (c) Total sum of seasons with data, out of a maximum of 472. (d) Mean annual gridbox uncertainty, defined as the mean gridbox error divided by its error in 1943.

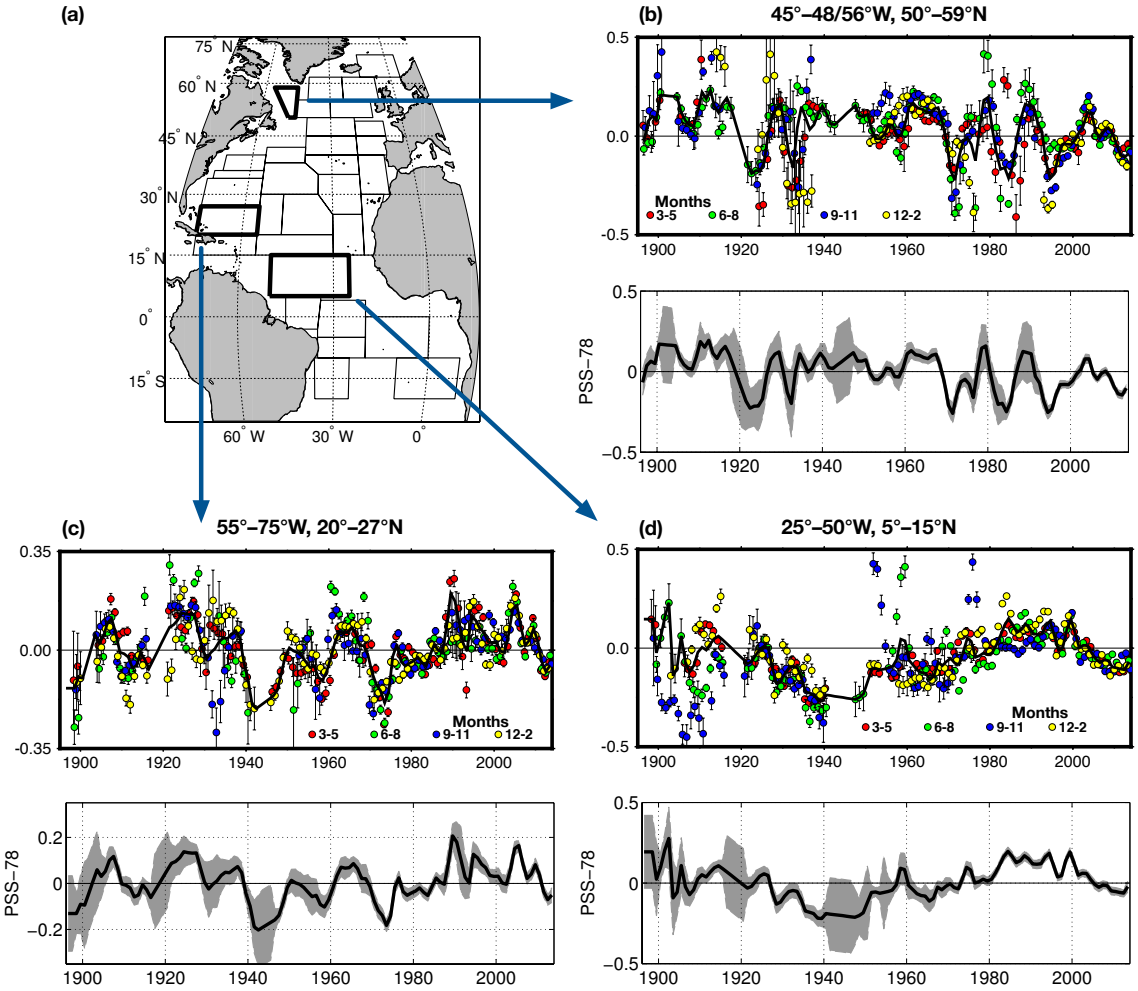

Figure S7: Examples of SSS time series construction in three grid boxes depicted in (a), in PSS-78: (b) Labrador Sea (45°–48/56°W, 50°–59°N), (c) western subtropical gyre (55°–75°W, 20°–27°N), and (d) ITCZ (25–50°W, 5–15°N). Top panels: Seasonally-binned median data (colored dots) with their estimated errors (error bars). The annual composite time series (1-2-1 filtered) is shown as the thick black line. Anomalies are from 1977–2013. Note that December–February is not included in the annual average time series in (b), and September–November is not included in (d). Bottom panels: annual (1-2-1 filtered) time series; shading indicates ± 2 standard error terms. These anomalies have been centered to the 1896–2013 baseline.